Optimal integration strategies for a syngas fuelled SOFC and gas turbine hybrid

Yingru Zhao [a,b], Jhuma Sadhukhan [c], Andrea Lanzini [d], Nigel Brandon [b], Nilay Shah [a,*]

[a] *Chemical Engineering, Imperial College London, London SW7 2AZ, UK*
[b] *Earth Science and Engineering, Imperial College London, London SW7 2AZ, UK*
[c] *Chemical Engineering, The University of Manchester, Manchester M13 9PL, UK*
[d] *Politecnico di Torino, Corso Duca degli Abruzzi 24, 10129 Torino, Italy*

A B S T R A C T

This article aims to develop a thermodynamic modelling and optimization framework for a thorough understanding of the optimal integration of fuel cell, gas turbine and other components in an ambient pressure SOFC–GT hybrid power plant. This method is based on the coupling of a syngas-fed SOFC model and an associated irreversible GT model, with an optimization algorithm developed using MATLAB to efficiently explore the range of possible operating conditions. Energy and entropy balance analysis has been carried out for the entire system to observe the irreversibility distribution within the plant and the contribution of different components. Based on the methodology developed, a comprehensive parametric analysis has been performed to explore the optimum system behavior, and predict the sensitivity of system performance to the variations in major design and operating parameters. The current density, operating temperature, fuel utilization and temperature gradient of the fuel cell, as well as the isentropic efficiencies and temperature ratio of the gas turbine cycle, together with three parameters related to the heat transfer between subsystems are all set to be controllable variables. Other factors affecting the hybrid efficiency have been further simulated and analysed. The model developed is able to predict the performance characteristics of a wide range of hybrid systems potentially sizing from 2000 to 2500 W m^{-2} with efficiencies varying between 50% and 60%. The analysis enables us to identify the system design tradeoffs, and therefore to determine better integration strategies for advanced SOFC–GT systems.

© 2011 Elsevier B.V. All rights reserved.

1. Introduction

To overcome the threats posed by climate change and energy security, advanced clean energy technologies are urgently needed. Hybrid fuel cell systems have emerged as attractive power generation solutions with great promise for high energy/power efficiency with reduced environmental emissions, allowing the shift from a fossil fuel-based economy to a new paradigm in a progressive manner [1,2]. Amongst the various types of fuel cell hybrids, the combination of solid oxide fuel cell (SOFC) and gas turbine (GT) has been identified as a key technology superior to many other options due to its fuel flexibility and ultra-high energy conversion efficiency [1–3]. To date several hybrid configurations have been presented or patented [4–6], along with theoretical studies which involve the thermodynamic analysis, design and performance modelling of SOFC–GT hybrids through individual and collaborative efforts [7–17].

In spite of the advantages of the SOFC–GT hybrid system, many technical barriers have to be overcome for the successful com-

mercial development of this power generation technology. These barriers are particularly evident in the smooth integration of the fuel cell and GT, since the GT has a strong coupling with the topping SOFC [18]. Therefore, design parameters need to be varied to determine performance sensitivity, and fundamental analysis is still needed to determine the practical operating constraints and the conditions for most efficient operation. Although there have already been a number of papers published in the area of hybrid SOFC–GT system analysis, most of them are generally focused on part-load or design point performance simulations instead of optimization. No optimization strategy has been proposed so far from a systematic integration perspective. Moreover, all the research formerly done was limited to either a particular system layout, or a particular operating or off-design condition.

System modelling combined with thermodynamic optimization can be a valuable tool in technological research, providing indications of technical feasibility, identifying ways to improve efficiency, and determining the best configuration and conditions for an integrated power plant [19]. To make a thorough investigation of the optimal integration amongst a fuel cell, gas turbine and other system components, a generic thermodynamic modelling and optimization framework is developed in the present study to systematically optimize the ambient pressure SOFC–GT

hybrid cycle as an important follow-up research effort based upon previous system modelling work. This methodology is based on the coupling of a coal syngas-fed SOFC model and an irreversible gas turbine cycle model, with an optimization algorithm developed using MATLAB to efficiently explore the range of possible operating conditions. In order to observe the irreversibility distribution within the plant and the contribution of different cycle components, a comprehensive energy and entropy balance analysis has been conducted for the entire system. Multi-irreversibilities coming from the electrochemical polarization, parasitic power consumption, finite-rate heat transfer, irreversible compression and expansion, and heat loss to the environment are all taken into account. The optimal efficiency and power density of the hybrid system have been deduced as a function of various system parameters. The current density, operating temperature, fuel utilization factor and temperature gradient of the fuel cell, as well as the isentropic efficiencies and temperature ratio of the gas turbine, together with two parameters related to the heat transfer between subsystems are all set to be controllable variables. Detailed numerical simulations have been performed to explore the optimum system behavior and parametric sensitivity analysis. It is important to notice that the approach presented here is based on an integrated multi-scale thermodynamic modelling and optimal design concept, which provides a new perspective to understand the hybrid fuel cell system with reduced complexity and enhanced generality. Therefore one of the most useful features of the methodologies is the ability to use the model to systematically evaluate the performance potential for a wide variety of configurations as well as the system design tradeoffs. This, in turn, assists the optimization and development of new energy technologies.

2. System configuration and description

The hybrid coupling derived from the integration of high temperature SOFC and gas turbine technology has been studied extensively [20], however, the prediction of the overall response of the system performance to the larger number of operating conditions remains a rather complex task. To develop an effective optimization strategy, it is important to understand the system design, component interactions and operating requirements.

2.1. System configuration

A fuel cell and a gas turbine may be configured in several different ways. They can be built to operate via either direct or indirect thermal coupling. Studies indicate that atmospheric system configurations, in which the thermal energy is utilized indirectly through a heat exchanger allowing the selection of GT pressure to be independent of the fuel cell pressure, would be less complex to develop and quicker to implement than pressurized ones. Since the fuel cell and gas turbine operate with different working fluids and at different pressures, the ambient pressure systems have the potential to be less expensive and could accommodate a wider variety of gas turbines as well as fuel cells [21]. For these reasons, an atmospheric system layout has been chosen to be examined in the present study. The basic concept of this SOFC–GT hybrid is depicted in Fig. 1, where the fuel cell acts as the core system component and generates most of the system power. Air is supplied by a blower and preheated prior to entry to the SOFC. The product gas of SOFC is sent into afterburner, where the un-reacted fuel is burnt with part of the excess air. Downstream of the fuel cell, the gas turbine is modelled as a compressor and a turbine mechanically linked via a common shaft, and thermodynamically coupled to the fuel cell via a primary heat exchanger (HEX1). The air leaving the compressor is heated up by the high-temperature exhaust gas of the fuel
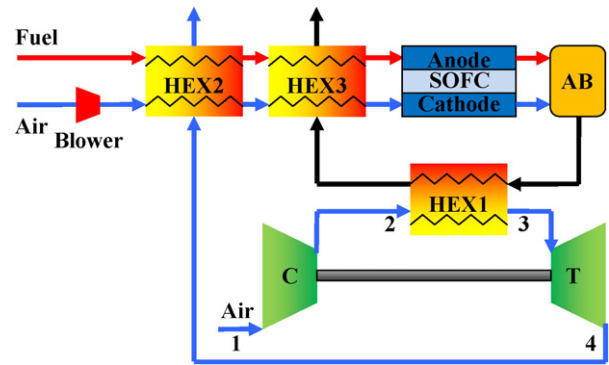

Fig. 1. The schematic diagram of an atmospheric SOFC–GT hybrid system.

cell which carries a significant amount of thermal energy. This hot air enters directly into the turbine and expands to produce power. As the most noticeable difference in configurations, two supplementary heat exchangers (HEX2 and HEX3) are adopted to serve as pre-heaters, recovering heat from both the exhaust gas of HEX1 and the turbine outlet for preheating the inlet air and fuel before they enter the fuel cell. The final exhaust gas rich in carbon dioxide from the hybrid system can be made capture ready after drying (water removal) and compression.

2.2. Model assumptions

Mathematical modelling is an essential tool for the analysis and design of energy conversion systems. This is particularly appropriate for the SOFC–GT hybrids, where localized experimental measurements are difficult due to the high operating temperature. To develop a mathematical model representing the electrochemical and thermodynamic characteristics of the entire system, a number of simplifications and assumptions are made to enable the analysis [7,19,21–30]:

- Both the fuel cell and gas turbine are assumed to be operated under steady-state conditions.
- Fuel cell reactions are assumed to be in equilibrium.
- Syngas consists of the following gas species, j = {H_2, CO, CH_4, CO_2, H_2O, N_2}.
- Air that enters the fuel cell consists of 79% N_2 and 21% O_2.
- The cathode and anode inlet temperature of the fuel cell are assumed to be equal.
- The cathode and anode exit temperature of the fuel cell are assumed to be equal.
- There is a temperature gradient (ΔT) across the SOFC. The temperature of the solid structure (T) is homogeneous and midway between the inlet and exit temperatures.
- All gases behave as ideal gases.
- Gas leakage is negligible.
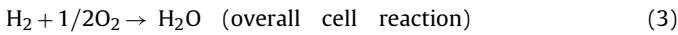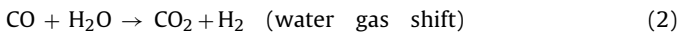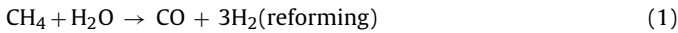- Heat loss to the environment occurs only in the fuel cell.

With the help of these assumptions, the system model will be constructed and the governing equations representing all modelled components of the hybrid cycle will be given in the following sections. Each of the system components are modelled individually and integrated to form the overall hybrid system.

3. Model formulation

3.1. Solid oxide fuel cell fuelled with coal syngas

SOFCs are devices that continuously convert chemical energy directly into electrical energy through electrochemical reactions. Various fuel options are feasible for SOFC operation [1,2]. H_2 is a traditional fuel gas, however, high purity H_2 is expensive and its cost will impede broad application of the SOFC. Coal derived syngas represents a more economical option given the abundance of the fuel as well as the development of gasification technology. It consists primarily of hydrogen and CO with significant water vapour and some levels of CO_2 and other minority species [31].

It is commonly assumed that only H_2 oxidation contributes to electrochemical power generation while CH_4 is reformed to carbon monoxide, which is then converted to CO_2 and H_2 through the water–gas shift reaction [3,20,22,32–34]. Consequently, the steam reforming reaction for methane, the water–gas shift reaction and electrochemical reactions occur simultaneously in the cell, and can be summarized as follows:

$$CH_4 + H_2O \rightarrow CO + 3H_2 \text{(reforming)} \tag{1}$$

$$CO + H_2O \rightarrow CO_2 + H_2 \quad \text{(water gas shift)} \tag{2}$$

$$H_2 + 1/2O_2 \rightarrow H_2O \quad \text{(overall cell reaction)} \tag{3}$$

Although a SOFC system may consist of several repeating electrochemical cells to reach technologically significant power levels, models of SOFCs are usually developed for the smallest unit-cell that is assumed to represent the operating conditions of the whole stack [23,27]. Thus a single SOFC cell simulation model is taken as representative that accounts for internal reforming and water–gas shift equilibrium, electrochemical polarizations and the associated heat generation, mass transfer via cell reactions, and overall energy balances [23,26,27]. This representation can be readily constructed as quantities such as stack voltage and stack power which are scaled versions of single-cell voltage and power.

3.1.1. Mass balances

In terms of the chemical and electrochemical reactions that occur within the anode and cathode of the SOFC, the first step is to calculate the equilibrium gas composition at the fuel and air channel exits.

The amount of hydrogen consumed in the fuel cell reactions, $\dot{n}_{H_2-c}$ (mol s^{-1}), is related to the current by Faraday's law [22,35,36]:

$$\upsilon = \dot{n}_{H_2-c} = \frac{iA}{n_e F} \tag{4}$$

where i denotes the current density, A represents the surface area of the interconnect plate (assuming the interconnect plates have the same area), n_e is the number of electrons transferred in reaction, and $F = 96,485$ C mol^{-1} is Faraday's constant. For a known fuel utilization factor, U_f, the amount of hydrogen supplied, $\dot{n}_{H_2-s}$ (mol s^{-1}), is given by

$$\dot{n}_{H_2-s} = \frac{\dot{n}_{H_2-c}}{U_f} = \frac{iA}{n_e F U_f} \tag{5}$$

The molar flow rate of the fuel stream, $\dot{n}_{f\text{-in}}$ (mol s^{-1}) needed to produce the required amount of hydrogen is thus

$$\dot{n}_{f\text{-in}} = \frac{\dot{n}_{H_2-s}}{x_{fc}} = \frac{iA}{n_e F U_f x_{fc}} \tag{6}$$

where x_{fc} is the number of moles of Hydrogen produced by 1 mol of fuel and it can be calculated according to the composition of the fuel as $x_{fc} = x_{H_2} + x_{CO} + 4x_{CH_4}$. For a known fuel gas composition x_j, its individual molar flow rate is:

$$\dot{n}_{f\text{-in}}(j) = \dot{n}_{f\text{-in}} x_j = \frac{iA x_j}{n_e F U_f x_{fc}} \tag{7}$$

where j are the components in the fuel stream, i.e., $j = \{H_2, CO, CH_4, CO_2, H_2O, N_2\}$.

An amount of steam equivalent to twice the amount needed for the reforming and water–gas shift reactions is supplied in order to avoid carbon deposition [22]. The molar flow rate of steam needed, $\dot{n}_{H_2O}$ (mol s^{-1}) is thus

$$\dot{n}_{H_2O} = (\dot{n}_{f\text{-in}}(CO) + \dot{n}_{f\text{-in}}(CH_4) \times 2) \times 2 \tag{8}$$

The molar flow rate of additional steam supplied, $\dot{n}_{ADD}$ (mol s^{-1}) is thus given by

$$\begin{aligned} \dot{n}_{ADD} &= \dot{n}_{H_2O} - \dot{n}_{f\text{-in}}(H_2O) \\ &= (\dot{n}_{f\text{-in}}(CO) + \dot{n}_{f\text{-in}}(CH_4) \times 2) \times 2 - \dot{n}_{f\text{-in}}(H_2O) \end{aligned} \tag{9}$$

Therefore the total molar flow rate of the fuel stream entering the SOFC, $\dot{n}_f$ (mol s^{-1}), becomes

$$\dot{n}_f = \dot{n}_{f\text{-in}} + \dot{n}_{ADD} \tag{10}$$

For known conversions for the reforming and water shift reactions, the component flow rates in the fuel exit stream are given as

$$\dot{n}_{f\text{-out}}(H_2) = \dot{n}_{H_2-s} \times (1 - U_f) \tag{11}$$

$$\dot{n}_{f\text{-out}}(CO) = 0 \tag{12}$$

$$\dot{n}_{f\text{-out}}(CO_2) = \dot{n}_{f\text{-in}}(CO) + \dot{n}_{f\text{-in}}(CO_2) + \dot{n}_{f\text{-in}}(CH_4) \tag{13}$$

$$\dot{n}_{f\text{-out}}(CH_4) = 0 \tag{14}$$

$$\dot{n}_{f\text{-out}}(H_2O) = \frac{\dot{n}_{H_2O}}{2} + \dot{n}_{H_2-s} \times U_f \tag{15}$$

$$\dot{n}_{f\text{-out}}(N_2) = \dot{n}_{f\text{-in}}(N_2) \tag{16}$$

Given a known inlet composition, the molar flow rates for the air stream are:

$$\dot{n}_{a\text{-in}}(O_2) = \dot{n}_{H_2-s} \times \frac{U_f/2}{U_a} \tag{17}$$

$$\dot{n}_{a\text{-in}}(N_2) = \dot{n}_{a\text{-in}}(O_2) \times \frac{0.79}{0.21} \tag{18}$$

$$\dot{n}_{a\text{-out}}(O_2) = \dot{n}_{a\text{-in}}(O_2) \times (1 - U_a) \tag{19}$$

$$\dot{n}_{a\text{-out}}(N_2) = \dot{n}_{a\text{-in}}(N_2) \tag{20}$$

where U_a is the air utilization factor, the subscript 'f' refers to the fuel stream, the subscript 'a' to the air stream, the subscript 'in' to the fuel cell inlet and the subscript 'out' the fuel cell outlet.

3.1.2. Electrochemical descriptions

For a fuel cell, its theoretical open-circuit voltage depends on the gas composition and temperature at the cathode and anode, which can be determined by the Nernst equation given as follows [9,23,24,36]:

$$E = \frac{-\Delta g(T, p)}{n_e F} \tag{21}$$

Note here the molar Gibbs free energy change for the fuel cell reaction depends dramatically on the temperature (T) and partial pressures of reactants (p), i.e., $\Delta g(T, p) = \Delta g^\circ(T) - RT \ln(p_{H_2} p_{O_2}^{1/2} / p_{H_2O})$, where $R = 8.314$ J mol^{-1} K^{-1} is the universal gas constant, p_{H_2}, p_{O_2}, and p_{H_2O} are the partial pressures of reactants H_2, O_2, and H_2O, respectively. Note that $\Delta g^\circ(T) = \Delta h^\circ - T \Delta s^\circ$

stands for the molar Gibbs free energy change at $p_0 = 1$ atm which also depends on temperature [9,23,24,37].

While the Nernst potential represents the maximum theoretical reversible voltage of a fuel cell at the given conditions, the voltage of an operating cell is generally lower than this. As current is drawn from a fuel cell, the cell voltage falls due to internal resistances and overpotential losses. These losses are common to all types of fuel cells and cannot be eliminated [9,24,32]. Here, three types of polarizations, i.e., activation, ohmic and concentration, are considered and calculated through Eqs. (22)–(30).

(1) **Activation overpotentials** depend on the kinetics of the electrochemical reactions occurring at the anode and cathode [2]. According to the general Butler–Volmer equation [24,32], the respective activation overpotentials of the anode and cathode can be calculated as [24,38,39]:

$$V_{\text{act},a} = \frac{2RT}{n_e F}\sinh^{-1}\left(\frac{i}{2i_{0,a}}\right) \tag{22}$$

$$V_{\text{act},c} = \frac{2RT}{n_e F}\sinh^{-1}\left(\frac{i}{2i_{0,c}}\right) \tag{23}$$

where $i_{0,a/c}$ denotes the anode/cathode exchange current density [32,37,40].

(2) **Ohmic overpotentials** are caused mostly by resistance to conduction of ions (through the electrolyte) and electrons (through the electrodes and current collectors) and by contact resistance between cell components [1,2]. The Ohmic losses in the present study are simulated by means of resistivity, obtained by the experimental temperature-dependent correlations [38,39]. Such resistances are summated as follows assuming a series electrical scheme:

$$V_{\text{ohm}} = I\sum_k R_k = iA\sum_k \frac{L_k}{\sigma_k A} = i\sum_k \frac{L_k}{\sigma_k} = i\left(\frac{L_e}{\sigma_e} + \frac{L_a}{\sigma_a} + \frac{L_c}{\sigma_c} + \frac{L_{\text{int}}}{\sigma_{\text{int}}}\right) \tag{24}$$

where R_k represents the resistance, L_k the thickness, A_k the area, and σ_k denotes the electronic conductivity of the anode, cathode, interconnect and the ionic conductivity of the electrolyte:

$$\sigma_e = C_{1e}\exp\left(\frac{C_{2e}}{T}\right) \tag{25}$$

$$\sigma_a = \frac{C_{1a}}{T}\exp\left(\frac{C_{2a}}{T}\right) \tag{26}$$

$$\sigma_c = \frac{C_{1c}}{T}\exp\left(\frac{C_{2c}}{T}\right) \tag{27}$$

$$\sigma_{\text{int}} = \frac{C_{1\text{int}}}{T}\exp\left(\frac{C_{2\text{int}}}{T}\right) \tag{28}$$

where C_{1e}–$C_{2\text{int}}$ are constants defined in Refs. [38,39] and shown in Table 1. The subscripts a, c, e and int denote anode, cathode, electrolyte and interconnect, respectively.

(3) **Concentration overpotentials** are the voltage drop due to mass transfer limitations from the gas phase into and through the electrode [24]. Previous papers based on such models showed that the resulting limiting current density is only slightly dependent on the SOFC temperature [41]. Thus, the concentration overvoltage calculation in the present study is simplified assuming a constant value for the limiting current density [7,19,32,40], evaluated as follows:

Table 1
Operating conditions and major parameters [8,16,20,22,34,37,40].

Parameter	Symbol	Value
Ambient temperature (K)	T_0	298
Operating pressure (atm)	p_0	1
Fuel utilization	U_f	0.8
Air utilization	U_a	0.2
Number of electrons	n_e	2
Anode exchange current density (A m^{-2})	$i_{0,a}$	6500
Cathode exchange current density (A m^{-2})	$i_{0,c}$	2500
Limiting current density (A m^{-2})	i_L	9000
Anode thickness (μm)	L_a	500
Anode conductivity constants	C_{1a}; C_{2a}	95×10^6; −1150
Cathode thickness (μm)	L_c	50
Cathode conductivity constants	C_{1c}; C_{2c}	42×10^6; −1200
Electrolyte thickness (μm)	L_e	10
Electrolyte conductivity constants	C_{1e}; C_{2e}	3.34×10^4; −10,300
Interconnect thickness (cm)	L_{int}	0.3
Interconnect conductivity constants	$C_{1\text{int}}$; $C_{2\text{int}}$	9.3×10^6; −1100
Compressor isentropic efficiency	η_c	90%
Turbine isentropic efficiency	η_e	93%
Air blower power consumption factor	η_{ab}	10%

$$V_{\text{conc},a} = -\frac{RT}{n_e F}\ln\left(1 - \frac{i}{i_{L,a}}\right) \tag{29}$$

$$V_{\text{conc},c} = -\frac{RT}{n_e F}\ln\left(1 - \frac{i}{i_{L,c}}\right) \tag{30}$$

where $i_{L,a/c}$ denotes the limiting current density of the anode/cathode.

Consequently, the terminal voltage of the SOFC can be obtained as follows:

$$V = E - V_{\text{act}} - V_{\text{ohm}} - V_{\text{conc}} = E - \frac{RT}{n_e F}d_1 \tag{31}$$

where $d_1 = 2\sinh^{-1}[i/(2i_{0,a})] + 2\sinh^{-1}[i/(2i_{0,c})] - \ln(1 - i/i_{L,a}) - \ln(1 - i/i_{L,c}) + [in_e F/(RT)](L_e/\sigma_e + L_a/\sigma_a + L_c/\sigma_c + L_{\text{int}}/\sigma_{\text{int}})$. The electrochemical performance of the fuel cell is described by plotting the terminal voltage versus the current density and operating temperature as shown in Fig. 3.

3.1.3. Air blower

Blowers play key roles in fuel cell designs. SOFC systems require blowers to provide motive force to the incoming atmospheric air, in order to overcome the pressure drop in the fuel cell stack and drive the air through the system. The electrical power required to drive this component is typically one of the largest parasitic loads for the fuel cell system, and one that, if not carefully designed to meet the external power demand, can lower the overall system efficiency [22,23,28,42].

A simple blower model is derived as follows to determine the power required for blowing air in the fuel cell section:

$$P_{ab} = P_{fc}\eta_{ab} \tag{32}$$

where η_{ab}, the power consumption factor, is defined as a ratio of the power provided by the fuel cell itself for air blowing to the total amount of power generated by the SOFC, and its value is normally no more than 20% [42–44]. Obviously the lower value of η_{ab}, the less power supplied to the air blower as parasitic losses, and the more net power this hybrid system would generate, resulting in a better hybrid performance.

3.1.4. Combustor

Because only part of the fuel can be oxidized in the SOFC, an afterburner is needed to combust the residuals and produce additional thermal energy for use elsewhere in the system. Therefore, the role of the combustor in the hybrid system under study is to

burn the non-reacted hydrogen coming out on the anode side of the fuel cell with the non-reacted oxygen exiting the cathode side.

Using a mass and energy balance on the combustor, a model is developed to determine the flow-rate and temperature of the combustor exit stream, given known values for the inlet streams:

$$\dot{n}_{c\text{-out}}(H_2) = 0 \tag{33}$$

$$\dot{n}_{c\text{-out}}(CO) = 0 \tag{34}$$

$$\dot{n}_{c\text{-out}}(CO_2) = \dot{n}_{f\text{-out}}(CO_2) \tag{35}$$

$$\dot{n}_{c\text{-out}}(CH_4) = 0 \tag{36}$$

$$\dot{n}_{c\text{-out}}(H_2O) = \dot{n}_{f\text{-out}}(H_2O) + \dot{n}_{f\text{-out}}(H_2) \tag{37}$$

$$\dot{n}_{c\text{-out}}(N_2) = \dot{n}_{f\text{-out}}(N_2) + \dot{n}_{a\text{-out}}(N_2) \tag{38}$$

$$\dot{n}_{c\text{-out}}(O_2) = \dot{n}_{a\text{-out}}(O_2) - \frac{\dot{n}_{f\text{-out}}(H_2)}{2} \tag{39}$$

Given all flow-rates, the temperature of the combustor exit stream (T_c) can be further determined by solving the energy balance equation of the combustor:

$$\dot{H}_{f\text{-out}}(T_{f\text{-out}}) + \dot{H}_{a\text{-out}}(T_{a\text{-out}}) = \dot{H}_{c\text{-out}}(T_c) \tag{40}$$

where $T_{f\text{-out}} = T_{a\text{-out}} = T + \Delta T/2$. Eq. (40) implies that the combustor exit temperature T_c is a function of the fuel cell temperature T.

3.1.5. Energy balances

Assuming ideal gas behavior, the enthalpy of a stream (W), $\dot{H}$, is calculated as a function of the molar flow rates and temperature [22] by

$$\dot{H} = \sum_i \dot{n}_i h_i(T) = \sum_i \dot{n}_i \left(\Delta h_i^\circ + \int_{T_0}^{T} c_{p,i}\, dT \right) \tag{41}$$

where the molar enthalpy of each species i in the stream, $h_i(T)$, is given as a function of the local temperature, with Δh_i° being the standard enthalpy change of formation of species i (J mol^{-1}) and $c_{p,i}$ denoting the heat capacity of component i (J mol^{-1} K^{-1}). Detailed polynomial fitting functions for the enthalpies, specific heats, entropies and Gibbs free energy values are evaluated based on temperature, according to the thermodynamic property data available from the literature [45–47].

Therefore, the total enthalpy change for the fuel cell section can be determined as:

$$\Delta \dot{H} = (-\Delta \dot{H}_{\text{preheater}}) + \Delta \dot{H}_{\text{SOFC}} = \frac{iA}{n_e F}(-\Delta h_{\text{preheater}} + \Delta h_{\text{SOFC}})$$

$$= \frac{iA}{n_e F} \Delta h \tag{42}$$

where $\Delta \dot{H}_{\text{preheater}}$ denotes the enthalpy change of the endothermic preheating process, and $\Delta \dot{H}_{\text{SOFC}}$ represents the enthalpy change for the overall exothermic electrochemical reaction. $\Delta h = -\Delta h_{\text{preheater}} + \Delta h_{\text{SOFC}}$ while $\Delta h_{\text{preheater}}$ and Δh_{SOFC} are expressions given in Appendix A.

Considering the electrochemical irreversible losses yields the rate of the total entropy production of the SOFC as

$$\dot{S}_{\text{tot}} = \frac{I(V_{\text{act}} + V_{\text{ohm}} + V_{\text{conc}})}{T_0} \tag{43}$$

where T_0 is the ambient temperature. Based on this, the net power output of the fuel cell can be deduced as a function of current density, temperature, partial pressures, chemical composition, and geometric/material characteristics as:

$$P_{fc} = -\Delta \dot{G} - T_0 \dot{S}_{\text{tot}} - P_{ab} = \frac{iA(-\Delta g - RTd_1)}{n_e F(1 + \eta_{ab})} \tag{44}$$
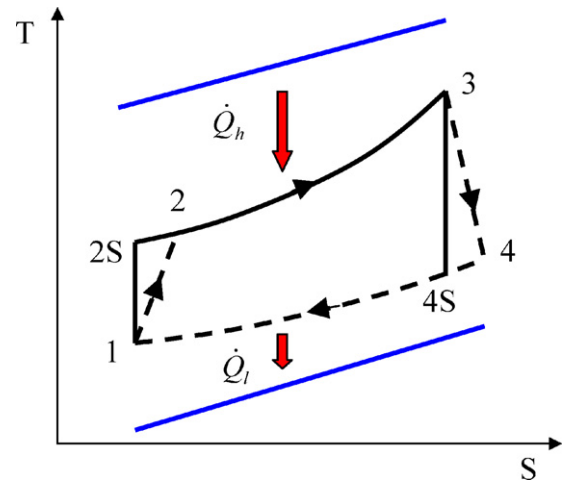

Fig. 2. The T–S diagram of an irreversible Brayton cycle.

where P_{ab} accounts for the parasitic electrical consumption in the air blower which is covered by the electricity generated by the fuel cell. As for the efficiency, it is defined as the power output divided by the total energy input:

$$\eta_{fc} = \frac{P_{fc}}{-\Delta \dot{H}} = \frac{-\Delta g - RTd_1}{-\Delta h(1 + \eta_{ab})} \tag{45}$$

Note that the simulation of a single cell unit is taken as representative of the entire stack performance.

3.2. Gas turbine and heat exchangers

3.2.1. Irreversible Brayton cycle

Gas turbines are power machines in which the working fluid is compressed, heated, and expanded for the purpose of generating power [48]. The basic thermodynamic cycle which describes steady-state and steady-flow energy characteristics of gas turbine components is known as the Brayton cycle [48]. An irreversible Brayton cycle is depicted in Fig. 2, where process 1–2S is an isentropic compression representing the power used by an ideal compressor, while process 1–2 takes into account the non-isentropic nature of a real compressor. Process 2–3 is the isobaric heat addition and process 4–1 is an isobaric heat rejection. The process 3–4S is an isentropic expansion representing the power output from an ideal turbine, while process 3–4 takes into account the non-isentropic nature of a real turbine. $T_i(i = 1, 2, 3, 4)$ is the temperature of the working fluid in the gas turbine at state points 1, 2, 3, and 4. $\dot{Q}_h$ and $\dot{Q}_l$ denote the heat flow transferred via HEX1 and HEX2, respectively. In the present paper, a practical irreversible cycle consisting of states 1–2–3–4–1 is considered.

To describe the irreversibility of a practical gas turbine cycle, the isentropic efficiencies of the compressor and turbine are introduced as controllable parameters [49,50]:

$$\eta_c = \frac{T_{2S} - T_1}{T_2 - T_1} \tag{46}$$

$$\eta_e = \frac{T_3 - T_4}{T_3 - T_{4S}} \tag{47}$$

When $\eta_c = 1$ and $\eta_e = 1$, $T_2 = T_{2S}$, $T_4 = T_{4S}$, and the irreversible compression and expansion processes become reversible. According to the adiabatic equations of an ideal gas and the characteristics of the Brayton cycle:

$$\frac{T_3}{T_{2S}} = \frac{T_{4S}}{T_1} \tag{48}$$
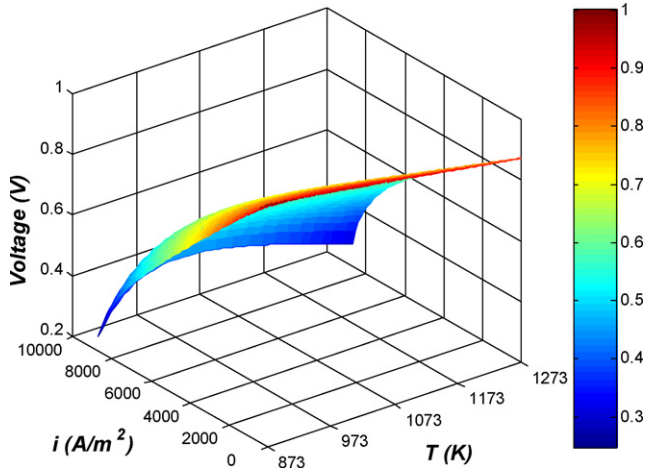
Fig. 3. The fuel cell terminal voltage varying with current density (i) and operating temperature (T), where the relevant parameters are listed in Tables 1 and 2.

the turbine outlet temperature can be readily deduced from Eqs. (46)–(48) as:

$$T_4 = (1 - \eta_e)T_3 + \frac{x\eta_e T_1}{\eta_c + x(1 - \eta_c)(T_1/T_3)} \qquad (49)$$

where $x = T_3/T_2$ is defined as the temperature ratio of the isobaric process 2–3, namely, the ratio of turbine inlet temperature to compressor exit temperature. Note that instead of using turbine inlet temperature as an operating parameter [8,21,51], this study has introduced x as a major controllable variable to determine the contribution of GT cycle components on the entire system performance.

3.2.2. Heat exchangers

As illustrated in Fig. 1, three heat exchangers are utilized in the system, all of which are modelled as flat plate counter flow heat exchangers as presented in Refs. [9,52]. The primary heat exchanger

(HEX1), which plays a vital role in the hybrid cycle, is used to recover the heat of the high temperature fuel cell exhaust to drive the bottoming gas turbine. Moreover, fuel and air pre-heaters are required, as the fuel cell does not tolerate a gas supply at low temperatures because of the excessive cooling and consequent thermal stresses that cold streams would cause. Therefore, two additional heat exchangers (HEX2 and HEX3) are further adopted to fully recycle the waste heat of the system and preheat the fuel cell incoming reactants in two steps. The heat transfer processes involved in the two pre-heaters are assumed to be ideal for the sake of simplicity.

As a main source of irreversibility, the loss caused by the finite-rate heat transfer between the SOFC and GT subsystems is considered. Once the finite heat transfer rate is taken into account, the performance of the gas turbine is closely dependent on heat-transfer laws. According to Newtonian heat-transfer [53] and the expression of log mean temperature difference (LMTD) [54], the heat transfer rates for the counter-flow heat exchanger, $\dot{Q}_h$ and $\dot{Q}_l$, can be expressed as

$$\dot{Q}_h = \dot{m}c_p(T_3 - T_2) = \frac{U_1 A_1[T_c - T + \Delta T/2 - T_3(1 - 1/x)]}{\ln u} \qquad (50)$$

$$\dot{Q}_l = \dot{m}c_p(T_4 - T_1) = \frac{U_2 A_2[1 + T_0 - (1 - \eta_e)T_3 - vT_1]}{\ln\{1/[(1 - \eta_e)T_3 + vT_1 - T_0]\}} \qquad (51)$$

where $u = (T_c - T_3)/(T - \Delta T/2 - T_3/x)$, $v = x\eta_e/[\eta_c + x(1 - \eta_c)(T_1/T_3)]$, $\dot{m}$ and c_p denote, respectively, the mass flow rate and heat capacity at constant pressure of the working fluid in the gas turbine, U_1 and U_2 are the heat transfer coefficients of HEX1 and HEX2, A_1 and A_2 represent the corresponding heat transfer surface areas.

Apart from the irreversibility existing in heat exchangers, the other major loss is due to heat lost from the SOFC directly to the environment. Heat loss is modelled based on the temperature difference between the fuel cell and ambient conditions as follows [7,19,55]:

$$\dot{Q}_{\text{loss}} = KA_l(T - T_0) \qquad (52)$$
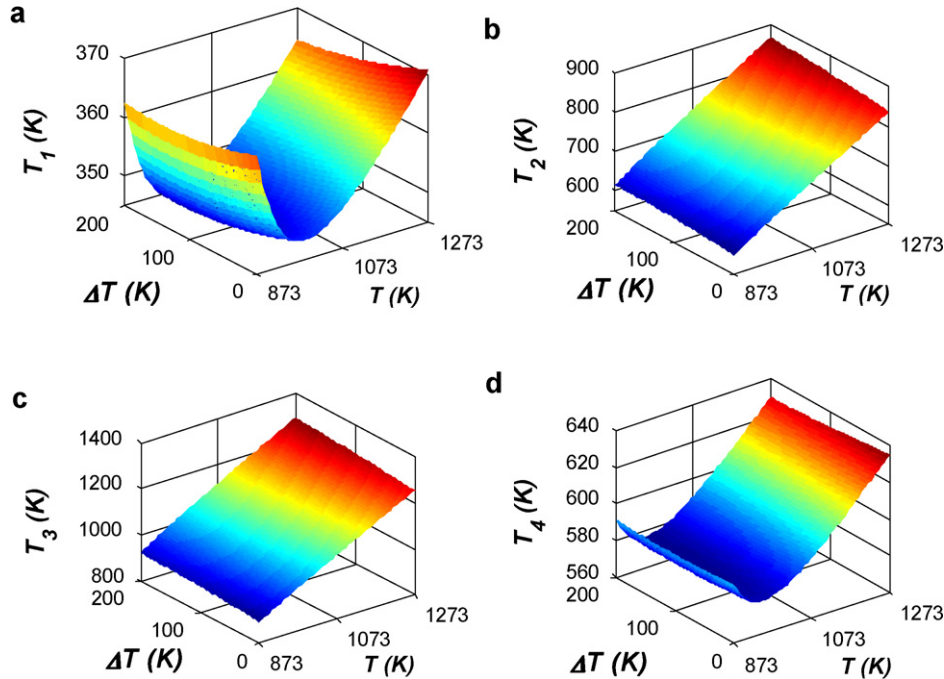
Fig. 4. The optimized GT temperatures varying with the operating temperature (T) and temperature difference (ΔT) of the fuel cell, where the parameters $i = 2000 \, \text{A m}^{-2}$, $x = 1.5$, $m_1 = 1.1$, $m_2 = -1.2 \times 10^{-7}$, and $m_3 = 0.01$ are chosen. The values of other parameters are listed in Tables 1 and 2.

where K represents the effective convective and/or conductive heat-leak coefficient, and A_l denotes the effective heat-transfer area. Note that this equation captures the effects of fuel cell temperature changes. Based on this, the heat flow rates transferred from the SOFC to the gas turbine can be obtained:

$$\dot{Q}_h = -\Delta\dot{H} - P_{fc} - \dot{Q}_{loss} = -\Delta\dot{H}(1-\eta_{fc}) - KA_l(T-T_0) \tag{53}$$

Therefore the efficiency of the gas turbine cycle can be expressed as

$$\eta_{gt} = 1 - \frac{\dot{Q}_l}{\dot{Q}_h} = 1 - \frac{\dot{m}c_p(T_4-T_1)}{\dot{m}c_p(T_3-T_2)} = 1 - \frac{(1-\eta_e)T_3 + vT_1 - T_1}{T_3 - T_3/x} \tag{54a}$$

or

$$\eta_{gt} = 1 - \frac{\dot{Q}_l}{\dot{Q}_h} = 1 - \frac{A_h U_1(w-T_1)(1+T_0-w)[T_c-T+\Delta T/2 - T_3(1-1/x)]}{\dot{Q}_h\left\{(U_1/U_2)(w-T_1)[T_c-T+\Delta T/2 - T_3(1-1/x)]\ln[1/(w-T_0)] + T_3(1-1/x)(1+T_0-w)\ln u\right\}} \tag{54b}$$

where $w = (1-\eta_e)T_3 + vT_1$, and $A_h = A_1 + A_2$ is the total heat transfer surface area. Comparison of Eq. (54a) with Eq. (54b) yields the following relation:

$$\frac{A_h U_1 T_3(1-1/x)(1+T_0-w)[T_c-T+\Delta T/2 - T_3(1-1/x)]}{\dot{Q}_h\{(U_1/U_2)(w-T_1)[T_c-T+\Delta T/2 - T_3(1-1/x)]\ln[1/(w-T_0)] + T_3(1-1/x)(1+T_0-w)\ln u\}} = 1 \tag{55}$$

Eq. (55) indicates that T_1 is a function of T_3. Using the solution of T_1 in Eq. (55), we can eliminate T_1 from Eqs. (54a) and (54b). Therefore, the gas turbine efficiency becomes only a function of T_3, A_h and $\dot{Q}_h$ with other given parameters, i.e., $\eta_{gt} = \eta_{gt}(T_3, A_h, \dot{Q}_h)$. Accordingly, when $\dot{Q}_h$ (the amount of heat released from the fuel cell to the gas turbine) and A_h (the total heat transfer area of the gas turbine cycle) are given, using Eqs. (54a) and (54b) and their extremal conditions $(\partial\eta_{gt}/\partial T_3)_{A_h,\dot{Q}_h} = 0$, it can be proved that when the gas turbine efficiency attains its maximum, the relationship between the turbine inlet temperature T_3 and compressor inlet temperature T_1 is determined by the following equation:

$$\frac{[(1-1/x)(T_1-D_3)D_5 + D_4D_5D_8 + D_4D_8(T_1-D_3)]D_6 + D_4D_5(T_1-D_3)(D_{13}+D_{14})}{[D_4D_5(D_9+1) + D_4D_9(T_1-D_3)]D_6 - D_4D_5D_{15}(T_1-D_3)} = \frac{T_1}{T_3} \tag{56}$$

where D_1–D_{15} are expressions given in Appendix A.

Substituting the solution of T_1 from Eq. (56) into Eq. (55) enables us to determine the relationship of the optimized T_3 varying with T as illustrated in Fig. 4c, which shows that the optimized value of turbine inlet temperature is a monotonically increasing function of the fuel cell operating temperature for other given parameters.

Following the above procedure, the optimized GT efficiency η_{gt} becomes only a function of the fuel cell temperature T for a set of given parameters. Combining the above equations yields the optimum efficiency and power output of the gas turbine as:

$$\eta_{gt} = 1 - \frac{(w-T_1)(1+T_0-w)[T_c-T+\Delta T/2 - T_3(1-1/x)]}{[im_2\,\Delta h(1-\eta_{fc}) - m_3(T-T_0)]\{m_1(w-T_1)[T_c-T+\Delta T/2 - T_3(1-1/x)]\ln[1/(w-T_0)] + T_3(1-1/x)(1+T_0-w)\ln u\}} \tag{57}$$

$$P_{gt} = \dot{Q}_h\eta_{gt} = \eta_{gt}\left[-\frac{iA\,\Delta h}{n_eF}(1-\eta_{fc}) + \frac{Am_3}{n_eFm_2}(T-T_0)\right] \tag{58}$$

where $m_1 = U_1/U_2$, $m_2 = -A/(n_eFA_hU_1)$ and $m_3 = KA_l/(U_1A_h)$. Note here temperatures T_3 and T_1 are determined by simultaneously solving Eqs. (55) and (56). Eqs. (57) and (58) indicate that the optimized efficiency and power output of the SOFC-driven gas turbine are closely dependent on the design and operating parameters of the upstream fuel cell subsystem.

3.3. Hybrid efficiency and power output

Based on the joint solution of Eqs. (53)–(58), the following expressions of the optimized efficiency and power output for the entire SOFC–GT hybrid system can be obtained:

$$\eta_{hybrid} = \frac{P_{hybrid}}{-\Delta\dot{H}} = \eta_{fc} + \frac{P_{gt}}{-\Delta\dot{H}} = \eta_{fc} + \frac{\dot{Q}_h}{-\Delta\dot{H}}\cdot\eta_{gt}$$
$$= \eta_{fc} + \eta_{gt}\left[1 - \eta_{fc} - \frac{m_3(T-T_0)}{im_2\,\Delta h}\right] \tag{59}$$

$$P_{hybrid} = -\Delta\dot{H}\cdot\eta_{hybrid}$$
$$= -\frac{iA\,\Delta h}{n_eF}\left\{\eta_{fc} + \eta_{gt}\left[1 - \eta_{fc} - \frac{m_3(T-T_0)}{im_2\,\Delta h}\right]\right\} \tag{60}$$

It is clearly seen from Eqs. (59) and (60) that the efficiency and power output of the hybrid system are closely dependent

on the parameters related to the various irreversible losses, which include the irreversibilities within the fuel cell itself and originating from heat transfer due to convection/conduction in the combined SOFC–GT power plant. The model is based on the physics, chemistry and electrochemistry that govern the entire system, and is developed by resolving conservation of mass and energy principles.

4. Parametric optimization analysis

In order to determine the sensitivity of the overall hybrid performance to the typical component parameters and to explore the optimum system operation, numerical simulations of this combined SOFC–GT power plant are carried out using MATLAB. The simulation model is based on a number of parameters, dramatically affecting the results coming out from the code.

The model easily allows changes and parameterization of any variable in it. For example, the fuel cell current density (i), operating temperature (T), temperature difference (ΔT), fuel utilization factor (U_f), air blower power consumption factor (η_{ab}), the GT temperature ratio (x) and isentropic efficiencies (η_c and η_e), as well as the synthesized parameters related to the finite-rate heat transfer via heat exchangers (m_1 and m_2), etc., are treated as independent design parameters that can individually be varied. For purpose of validation, the overall performance is predicted by the present model based on the validated data adopted from previous literature [8,20,24,26,38,41,44,56]. Values of those parameters are summarized in Tables 1 and 2, and are used as constants throughout the study unless mentioned specifically.

Table 2
Coal syngas composition [52].

Components	Mole fractions
H_2	0.293
CO	0.287
CO_2	0.118
CH_4	0.000
N_2	0.030
H_2O	0.272

In particular, some operating constraints have been considered in order to determine a more generalized system. For example, the fuel cell temperature rise, i.e., the temperature difference between the SOFC inlet and outlet, must remain below 200 K to minimize thermal stresses in a practical fuel cell since its tri-layer materials are ceramics which are not capable of withstanding the thermal stresses associated with larger temperature gradients [23]. Thus, a temperature difference greater than 200 K is excluded from the practical design range. As for the range of fuel utilizations considered, although fuel cell efficiency continuously increases with increasing fuel utilization, utilizations of 90% and above are not practically achievable due to imperfect fuel distribution and the need for a margin of safety [23]. Therefore the average fuel utilization selected for most of the simulation in this paper is 80%. Moreover, as a synthesized parameter to measure the effect of heat loss irreversibility on the system performance, different values of m_3 correspond to different quantities of energy released by the system as heat loss to the environment. A value of 0.01 for m_3 is found to result in approximately 7–9% heat loss with respect to the total energy input of the system at typical operating conditions, which is quite reasonable according to previous studies [23]. Hence this value is chosen for m_3 throughout the simulation analysis.

Using Eqs. (59) and (60), as well as the solutions of T_3 and T_1 which are determined by the simultaneous Eqs. (55) and (56), enables us to plot the efficiency and power density of the optimized SOFC–GT system varying with the fuel cell current density and operating temperature, as presented in Fig. 5, where the power density $P^*_{hybrid} = P_{hybrid}/A$. The meshes are generated over a specified temperature domain of 873–1273 K and a current density domain of 1800–2200 A m^{-2} because the SOFC generally operates within these ranges [8,51]. It is interesting to observe that the hybrid efficiency passes through a maximum value when the SOFC temperature is varied, while the hybrid power density increases monotonically with increasing temperature. Therefore there exists an optimum T_{opt} which denotes the corresponding temperature when the hybrid efficiency attains its maximum η_{max}. This is different from the cases reported in Refs. [21,23] that indicated monotonically increasing efficiency of the hybrid system with increasing fuel cell temperature. On the other hand, when the current density of the fuel cell is increased from 1800 to 2200 A m^{-2}, the hybrid efficiency will decrease monotonically while there exists a maximum power output P_{max} with i_{opt} being the corresponding optimum current density. Note here the behavior of system efficiency is consistent with most of the cases for SOFC–GT hybrids [23,57–59]. Furthermore, T_{opt} will decrease with the increase in fuel cell current density, while i_{opt} increases as the fuel cell temperature is increased.

The advantage of the hybrid configuration can be better illustrated by comparing its performance with that of the SOFC only or GT only system. As shown in Fig. 6, under typical operating conditions the maximum hybrid power density is 2300 W m^{-2}, about 68% of that is from the SOFC and 32% is from GT. The maximum efficiency of the hybrid system is 57%, which is 15% higher than that of the SOFC only system and 19% higher than the GT only system.
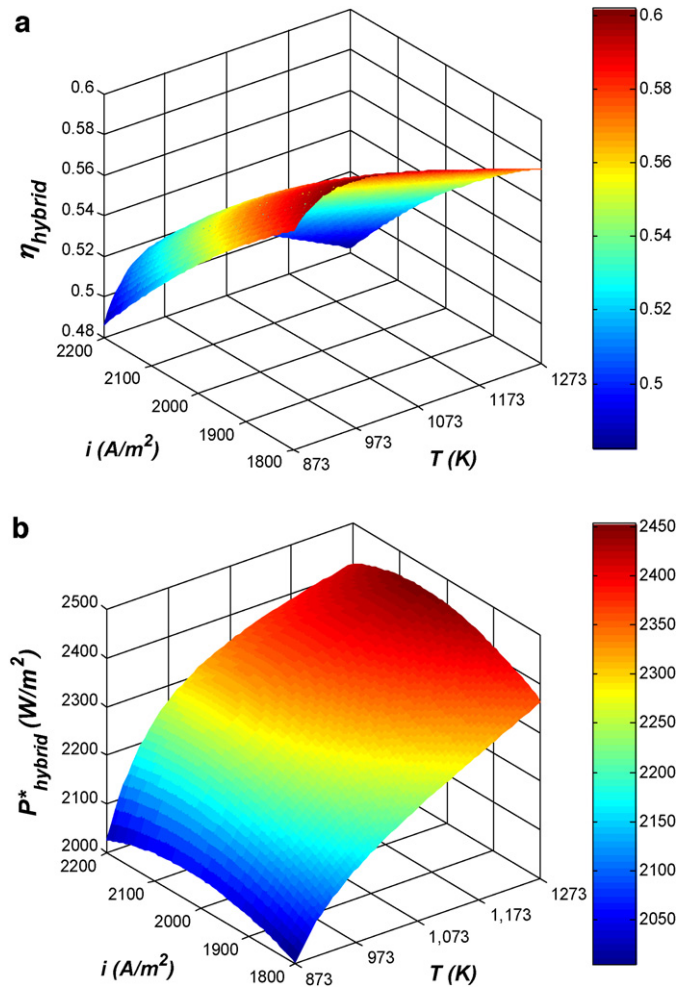
Fig. 5. The system efficiency (a) and power density (b) of the hybrid SOFC–GT system varying with the operating temperature (T) and current density (i) of the fuel cell, where the parameters $\Delta T = 100$ K, $x = 1.5$, $m_1 = 1.1$, $m_2 = -1.2 \times 10^{-7}$, and $m_3 = 0.01$ are chosen. The values of other parameters are listed in Tables 1 and 2.

Accordingly, having established the baseline performance, more selected system parameters will be varied and the sensitivity of these parameters to the hybrid performance will be evaluated in the following sections.

4.1. Influence of temperature

In a hybrid system, temperatures of different components are strongly coupled. Therefore, knowledge of the prime temperature-related parameters is required. There are four major temperature parameters: the turbine inlet temperature (T_3), the fuel cell operating temperature (T), the GT temperature ratio (x), and the temperature difference across the fuel cell (ΔT). Only three of them can be selected as independent parameters and the remaining parameter is obtained from the analysis [21]. In the present study, T, ΔT and x are set as the independent design parameters and the turbine inlet temperature, i.e., T_3, is determined from the optimization procedure as described above.

To illustrate how the SOFC temperature affects the GT cycle, Fig. 4 has been plotted to show the sensitivity of the GT temperatures to the operating temperature and temperature difference of the fuel cell. As shown in Fig. 4c, increasing the fuel cell temperature (T) tends to increase the turbine inlet temperature (T_3). For a given GT temperature ratio (x), this would of course result in an increased compressor exit temperature (T_2) as seen from Fig. 4b.
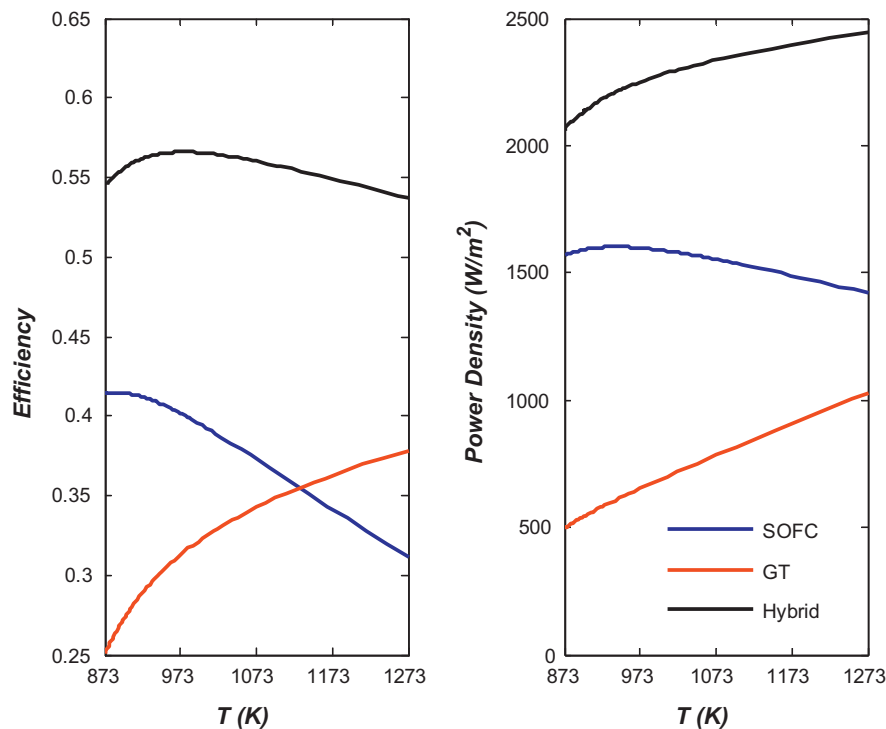
Fig. 6. The efficiency and power density comparisons between SOFC, GT and hybrid system, where the parameters $i = 2000\,\text{A m}^{-2}$, $\Delta T = 100\,\text{K}$, $x = 1.5$, $m_1 = 1.1$, $m_2 = -1.2 \times 10^{-7}$, and $m_3 = 0.01$ are chosen. The values of other relevant parameters are listed in Tables 1 and 2.

Meanwhile, it is found that both the turbine outlet temperature (T_4) and the compressor inlet temperature (T_1) will first decrease and then increase with an increasing T, which can be further explained by Eqs. (49), (55) and (56). On the other hand, the variation in the fuel cell temperature difference seems to have a relatively small effect on the GT temperatures. As shown in Fig. 4, both T_2 and T_3 will increase with an increasing ΔT, while both T_1 and T_4 will decrease as ΔT is increased, although these variations are not very obvious.

The effect of SOFC operating temperature on the hybrid performance can be further explained by the curves in Figs. 3–6. As previously shown in Fig. 5, the hybrid efficiency will pass through a maximum value while the power density only increases monotonically and quickly with an increase in T. This is due to many reasons. Firstly, the fuel cell terminal voltage with respect to temperature rise has a peak instead of a monotonically changing trend according to Fig. 3. Hence for a given current density, maximum values of the power density and cell efficiency are achievable, shown by the blue curves in Fig. 6. At the same time, increasing the fuel cell temperature leads to a greater GT power and efficiency as described by the red curves in Fig. 6. This is mainly because the turbine inlet temperature is directly increased with the fuel cell temperature rise, as can be readily seen from Fig. 4. When the fuel cell operates at a higher temperature its power contribution decreases, however, this reduction is compensated by a larger amount of power produced by the GT at higher temperature, thereby leading to an increase in the overall hybrid power output as shown by the black curve in Fig. 6. In addition, increasing the fuel cell temperature also means an increase in the total energy input of the hybrid system, which conclusively results in an optimal hybrid efficiency as described in Fig. 5. (For interpretation of the references to colour in this text, the reader is referred to the web version of the article.)

On the gas turbine side, its temperature ratio (x) is another independent design parameter. Concerning the sensitivity of the hybrid performance to the GT temperature ratio and fuel cell temperature difference, Fig. 7 provides a good example for the comparison of these two different parametric effects. According to the sim-

ulation results, the hybrid efficiency increases dramatically with increasing x, which is mainly due to the higher turbine inlet temperature and subsequently an increased GT power contribution. When more GT power is generated the total power output of the system will increase accordingly, and consequently the hybrid efficiency becomes higher. Compared to the effect of x, the hybrid efficiency remains almost constant when ΔT is varied. This is quite different from the conclusions of Refs. [21,23] which indicate a huge effect of ΔT on the system performance. Nevertheless, the slight reduction in the hybrid efficiency with decreasing ΔT is consistent with previous results [21]. The main cause is due to the lower turbine inlet temperature for a smaller ΔT and the resulting reduced power contribution of the gas turbine.
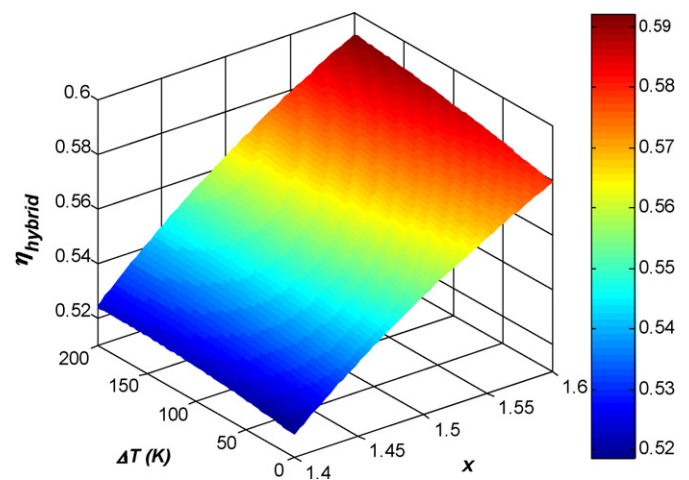
Fig. 7. The system efficiency of the hybrid SOFC–GT varying with the GT temperature ratio (x) and the fuel cell temperature difference (ΔT), where the parameters $i = 2000\,\text{A m}^{-2}$, $T = 1073\,\text{K}$, $m_1 = 1.1$, $m_2 = -1.2 \times 10^{-7}$, and $m_3 = 0.01$ are chosen. The values of other relevant parameters are listed in Tables 1 and 2.
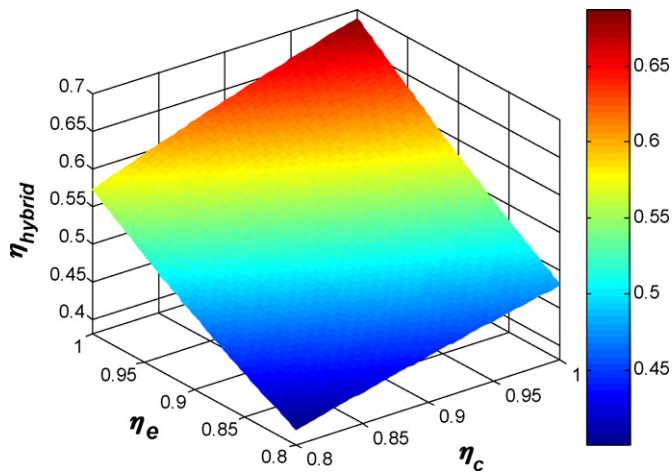
Fig. 8. The system efficiency of the hybrid SOFC–GT varying with the compressor isentropic efficiency (η_c) and the turbine isentropic efficiency (η_e), where the parameters $i = 2000 \, \text{A m}^{-2}$, $T = 1073 \, \text{K}$, $\Delta T = 100 \, \text{K}$, $x = 1.5$, $m_1 = 1.1$, $m_2 = -1.2 \times 10^{-7}$, and $m_3 = 0.01$ are chosen. The values of other relevant parameters are listed in Tables 1 and 2.

4.2. Influence of GT isentropic efficiencies

As seen in Fig. 8, the irreversibility in the adiabatic processes of the gas turbine cycle has great effect on the system performance. The hybrid efficiency will increase rapidly when either of the isentropic efficiencies of the compressor and turbine are increased. This is mainly due to the higher turbine inlet temperature and subsequently a raised GT power contribution that is caused by an increase in turbine and compressor efficiencies. However, it shows that the hybrid efficiency increases more significantly with the turbine isentropic efficiency (η_e) than the compressor isentropic efficiency (η_c). According to the simulation results, hybrid efficiency tends to increase by around 17% when η_e increases from 0.8 to 1, and this efficiency growth is 9% higher than that with an increasing η_c. It is noteworthy that such a high sensitivity of the system performance to changes in the GT expansion process has not been reported before. A better turbine design is obviously quite essential to enhance the entire hybrid SOFC–GT performance.

4.3. Influence of finite-rate heat transfer

The effect of irreversibilities due to finite-rate heat transfer on the system performance can be best explained by two parameters, m_1 and m_2.

As the ratio of heat transfer coefficients between two heat exchangers (HEX1 and HEX2), $m_1 = U_1/U_2$ is only to measure the performance of the GT cycle and is independent of the upstream SOFC subsystem. Fig. 9 shows clearly that the predicted hybrid efficiency will decrease as parameter m_1 is increased. This is because an increasing m_1 will lead to a lower turbine inlet temperature, which in turn results in a decreased GT power contribution. Thus due to the relatively smaller contribution of the gas turbine power the total system power is decreased, and accordingly the hybrid efficiency decreases.

On the contrary, the hybrid efficiency tends to increase rapidly with increasing m_2, which is a synthetic parameter to measure the irreversibility of finite-rate heat transfer in the gas turbine, as also illustrated in Fig. 9. This can be attributed to the higher turbine inlet temperature, and thus a bigger GT power contribution, resulting from an increased m_2.

In conclusion, a higher value of m_2 and a lower value of m_1 would lower heat transfer irreversibilities and thus improve hybrid performance.
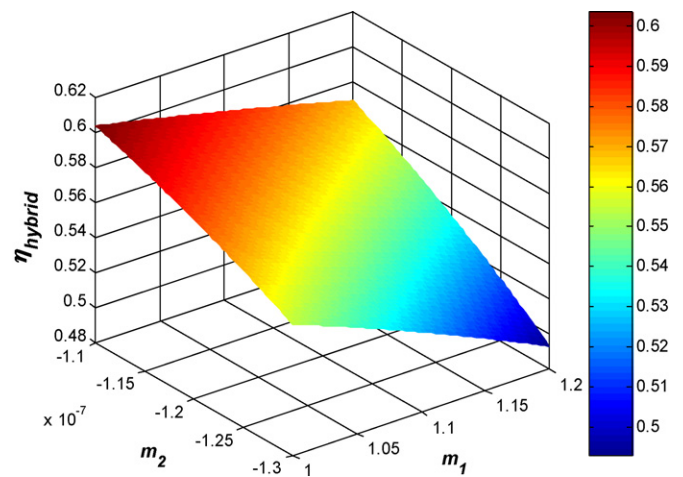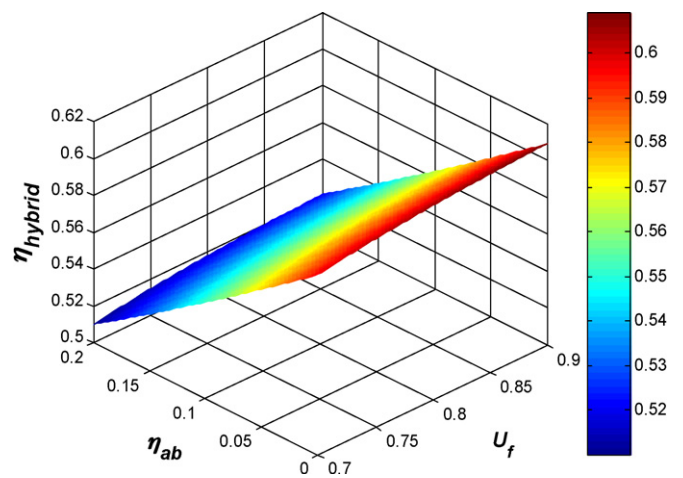

Fig. 9. The system efficiency of the hybrid SOFC–GT varying with m_1 and m_2, where the parameters $i = 2000 \, \text{A m}^{-2}$, $T = 1073 \, \text{K}$, $\Delta T = 100 \, \text{K}$, $x = 1.5$, and $m_3 = 0.01$ are chosen. The values of other relevant parameters are listed in Tables 1 and 2.

4.4. Influence of fuel utilization and electrical parasitic losses

As depicted visibly in Fig. 10, fuel utilization and electrical parasitic consumption both affect the performance of the combined SOFC–GT system. First, the hybrid efficiency tends to increase by only 1.5% when the fuel utilization factor (U_f) increases from 0.7 to 0.9. The slight increase is due to many reasons. First of all, when operating at higher fuel utilization factor, due to decreased inlet fuel flow rate, the SOFC works at lower voltage which in turn means reduced SOFC power contribution. However, higher fuel utilization would result in higher turbine inlet temperature, leading to increased GT power contribution. Hence, an enhanced overall hybrid efficiency is expected, illustrated in Fig. 10.

On the other hand, an increase by 9% in the hybrid efficiency is predicted when the power consumption factor of the air blower (η_{ab}) decreases from 20% to 0%, due to the decreased parasitic losses in the system.

Comparing the influence of these two factors, the magnitude for that of the parasitic losses is much more significant. Therefore, more effort should be put into the development of more efficient blowers to reduce the system parasitic losses.

Fig. 10. The system efficiency of the hybrid SOFC–GT varying with fuel utilization factor U_f and air blower power consumption factor η_{ab}, where the parameters $i = 2000 \, \text{A m}^{-2}$, $T = 1073 \, \text{K}$, $\Delta T = 100 \, \text{K}$, $x = 1.5$, $m_1 = 1.1$, $m_2 = -1.2 \times 10^{-7}$, and $m_3 = 0.01$ are chosen. The values of other relevant parameters are listed in Tables 1 and 2.

5. Conclusions

In this article, an integrated atmospheric syngas fueled SOFC–GT power plant has been examined. An optimization strategy applying a generalized theoretical model of this hybrid has been carried out through thermodynamic system modelling to determine the optimum integration between the fuel cell and gas turbine. The governing equations of energy conversion for each system component as well as the entire system have been developed. The overall system performance and the effect of varying design and control parameters have been predicted through a detailed parametric analysis, where the current density, operating temperature, fuel utilization factor and temperature gradient of the fuel cell, the isentropic efficiencies and temperature ratio of the gas turbine cycle, as well as the parameters related to the finite-rate heat transfer between subsystems are all set to be controllable variables.

The theoretical analyses have indicated that by selecting an optimal turbine inlet temperature according to the joint solution of Eqs. (55) and (56), the highest GT efficiency and the maximum power output will be achieved, which in turn implies an optimum integration between the fuel cell and the downstream gas turbine. In addition, the parametric analyses have identified a number of essential performance characteristics. For example, the impact of integrating a GT bottoming cycle is found to be significant, adding as much as 19% of efficiency to the system at typical operating conditions. Both the hybrid efficiency and power density will change dramatically with variations in the fuel cell current density and operating temperature over the ranges investigated. Particularly, the simulation results revealed that an increase in either compressor isentropic efficiency or turbine isentropic efficiency will lead to a significant improvement in the overall efficiency of the system,

$$
\begin{aligned}
\Delta h_{\mathrm{preheater}} = \ &\left\lfloor x_{\mathrm{H_2}} h_{\mathrm{H_2}}(T) + x_{\mathrm{CO}} h_{\mathrm{CO}}(T) + x_{\mathrm{CH_4}} h_{\mathrm{CH_4}}(T) + x_{\mathrm{CO_2}} h_{\mathrm{CO_2}}(T) + x_{\mathrm{N_2}} h_{\mathrm{N_2}}(T) + (2 x_{\mathrm{CO}} + 4 x_{\mathrm{CH_4}}) h_{\mathrm{H_2O}}(T) \right\rfloor / (U_f x_{fc}) \\
&+ \left[h_{\mathrm{O_2}}(T) + 3.7619 h_{\mathrm{N_2}}(T) \right] / (2 U_a) \\
&- \left[x_{\mathrm{H_2}} h_{\mathrm{H_2}}(T_0) + x_{\mathrm{CO}} h_{\mathrm{CO}}(T_0) + x_{\mathrm{CH_4}} h_{\mathrm{CH_4}}(T_0) + x_{\mathrm{CO_2}} h_{\mathrm{CO_2}}(T_0) + x_{\mathrm{N_2}} h_{\mathrm{N_2}}(T_0) + (2 x_{\mathrm{CO}} + 4 x_{\mathrm{CH_4}}) h_{\mathrm{H_2O}}(T_0) \right] / (U_f x_{fc}) \\
&- \left[h_{\mathrm{O_2}}(T_0) + 3.7619 h_{\mathrm{N_2}}(T_0) \right] / (2 U_a)
\end{aligned}
$$

$$
\begin{aligned}
\Delta h_{\mathrm{SOFC}} = \ &\left\lfloor (1 - U_f) x_{fc} \cdot h_{\mathrm{H_2}}(T) + (x_{\mathrm{CO}} + x_{\mathrm{CO_2}} + x_{\mathrm{CH_4}}) \cdot h_{\mathrm{CO_2}}(T) + (x_{\mathrm{CO}} + 2 x_{\mathrm{CH_4}} + U_f x_{fc}) \cdot h_{\mathrm{H_2O}}(T) + x_{\mathrm{N_2}} \cdot h_{\mathrm{N_2}}(T) \right\rfloor / (U_f x_{fc}) \\
&+ \left[(1 - U_a) h_{\mathrm{O_2}}(T) + 3.7619 h_{\mathrm{N_2}}(T) \right] / (2 U_a) \\
&- \left[x_{\mathrm{H_2}} h_{\mathrm{H_2}}(T) + x_{\mathrm{CO}} h_{\mathrm{CO}}(T) + x_{\mathrm{CH_4}} h_{\mathrm{CH_4}}(T) + x_{\mathrm{CO_2}} h_{\mathrm{CO_2}}(T) + x_{\mathrm{N_2}} h_{\mathrm{N_2}}(T) + (2 x_{\mathrm{CO}} + 4 x_{\mathrm{CH_4}}) h_{\mathrm{H_2O}}(T) \right] / (U_f x_{fc}) \\
&- \left[h_{\mathrm{O_2}}(T) + 3.7619 h_{\mathrm{N_2}}(T) \right] / (2 U_a)
\end{aligned}
$$

however, the hybrid efficiency is found to be relatively insensitive to the fuel utilization factor and the SOFC temperature gradient. On the other hand, a reduction of hybrid efficiency is found to be evident for a decrease in the GT temperature ratio. Other factors affecting the hybrid system has been further simulated, such as the electrical parasitic consumption, which also strongly affects the performance of the combined SOFC–GT system. For instance, an increase of 9% in the hybrid efficiency is predicted when the power consumption factor of the air blower decreases from 20% to 0%, indicating that effort should be put into the development of more efficient blowers to reduce the system parasitic losses. These interactions analyses can be used to determine the optimum system operation and thereby to derive useful design guidelines. It should be noted that the size of system is not defined in this paper, because the model developed here is a generic one which is able to predict the performance characteristics of a wide range of hybrid systems potentially sizing from 2000 to 2500 W m^{-2} with efficiencies varying roughly between 50% and 60%, as illustrated in the figures.

In summary, the hybrid SOFC–GT system is shown to be robust and thermodynamically stable over a wide range of operating conditions, and based on the optimization procedure this model is shown to give comparable performance predictions. The designed optimization strategy presented here provides valuable insights regarding design tradeoffs and optimal integration considerations for hybrid fuel cell power plants. To make the performance improvements potentially achievable, the analysis reveals that it is desirable to design such hybrid systems with the largest possible GT temperature ratio, the lowest possible parasitic losses, and moderate fuel cell current density and operating temperature.

Finally, this analysis will be the basis for a future determination of the system performance capability and robustness to fuel concentration variations by considering more complex models. To explore better optimization methodologies, the practical feasibility of such optimization procedures still needs to be investigated, and a more in-depth analysis of the system response to a larger number of decision variables than actually considered in the present study will be part of our ongoing research. The model would also benefit from validation against experimental data based around the cycles analysed here, though such data is lacking in the literature at present. Note that the performance characteristics presented herein may change significantly with various system configurations, and this is also a topic which should be considered for future studies.

Appendix A.

1. The expressions of $\Delta h_{\mathrm{preheater}}$ and Δh_{SOFC} in Eq. (42) are given as follows:

2. The expressions of D_1–D_{10} in Eq. (56) are listed as follows:

$$
D_1 = \frac{x \eta_e}{\eta_c + x(1 - \eta_c)(T_1/T_3)}
$$

$$
D_2 = \ln\left(\frac{T_c - T_3}{T - \Delta T/2 - T_3/x} \right)
$$

$$
D_3 = (1 - \eta_e) T_3 + D_1 T_1
$$

$$
D_4 = T_c - T + \frac{\Delta T}{2} - T_3 \left(1 - \frac{1}{x}\right)
$$

$$
D_5 = 1 + T_0 - D_3
$$

$$
D_6 = m_1 D_4 (D_3 - T_1) \ln\left(\frac{1}{D_3 - T_0}\right) + D_2 T_3 \left(1 - \frac{1}{x}\right)(1 + T_0 - D_3)
$$

$$
D_7 = i m_2 \Delta h (1 - \eta_{fc}) - m_3 (T - T_0)
$$

$$D_8 = 1 - \eta_e + \frac{(1-\eta_c)D_1^2(T_1/T_3)^2}{\eta_e}$$

$$D_9 = \frac{(1-\eta_c)D_1^2(T_1/T_3)}{\eta_e} - D_1$$

$$D_{10} = T - \frac{\Delta T}{2} - \frac{T_3}{x}$$

$$D_{11} = \frac{1}{D_3 - T_0}$$

$$D_{12} = \frac{D_5 T_3(1-1/x)[(T_c - T_3)/(D_{10}x) - 1]}{T_c - T_3}$$

$$D_{13} = m_1(T_1 - D_3)\left[\left(1 - \frac{1}{x}\right)\ln(D_{11}) + D_4 D_8 D_{11}\right]$$

$$D_{14} = m_1 D_4 D_8 \ln(D_{11}) + D_2\left(1 - \frac{1}{x}\right)(D_5 - D_8 T_3) + D_{12}$$

$$D_{15} = -m_1 D_4(D_9 + 1)\ln(D_{11}) - m_1 D_4 D_9 D_{11}(T_1 - D_3)$$
$$+ T_3\left(1 - \frac{1}{x}\right)D_2 D_9$$

References

[1] J. Larminie, A. Dicks, Fuel Cell Systems Explained, 2nd ed., Wiley, New York, 2003.
[2] S.C. Singhal, K. Kendall, High Temperature Solid Oxide Fuel Cells, Elsevier, 2003.
[3] X. Zhang, S.H. Chan, G. Li, H.K. Ho, J. Li, Z. Feng, Journal of Power Sources 195 (2010) 685–702.
[4] Fuel Cells Bulletin 11 (2003) 4–5.
[5] Fuel Cells Bulletin 10 (2006) 4.
[6] Fuel Cells Bulletin 1 (2007) 5–6.
[7] Y. Zhao, N. Shah, N. Brandon, Fuel Cells 10 (2010) 181–193.
[8] Y. Haseli, I. Dincer, G.F. Naterer, International Journal of Hydrogen Energy 33 (2008) 5811–5822.
[9] S.H. Chan, H.K. Ho, Y. Tian, International Journal of Hydrogen Energy 28 (2003) 889–900.
[10] A.V. Akkaya, B. Sahin, H.H. Erdem, International Journal of Hydrogen Energy 33 (2008) 2566–2577.
[11] C. Bao, Y. Shi, C. Li, N. Cai, Q. Su, International Journal of Hydrogen Energy 35 (2010) 2894–2899.
[12] P. Aguiar, D.J.L. Brett, N.P. Brandon, International Journal of Hydrogen Energy 33 (2008) 7214–7223.
[13] M.G. Pangalis, R.F. Martinez-Botas, N.P. Brandon, Proceeding of the Institution of Mechanical Engineers, Part A: Journal of Power and Energy 216 (2002) 129–144.
[14] A.F. Massardo, F. Lubelli, Journal of Engineering for Gas Turbines and Power 122 (2000) 27–35.
[15] A.F. Massardo, F. Lubelli, Journal of Engineering for Gas Turbines and Power 125 (2003) 67–74.
[16] G.T. Lee, F.A. Sudhoff, Proceedings of the Fuel Cells'96 Review Meeting, DOE/METC/C-97/7278, August 20, 1996.
[17] Y. Tsujikawa, K. Kaneko, J. Suzuki, JSME International Journal Series B 47 (2004) 256–260.
[18] T.H. Lim, R.H. Song, D.R. Shin, J.I. Yang, H. Jung, I.C. Vinke, S.S. Yang, International Journal of Hydrogen Energy 33 (2008) 1076–1083.
[19] Y. Zhao, N. Shah, N. Brandon, International Journal of Hydrogen Energy, in press, doi:10.1016/j.ijhydene.2010.11.015.
[20] M. Granovskii, I. Dincer, M.A. Rosen, Journal of Power Sources 165 (2007) 307–314.
[21] S.K. Park, T.S. Kim, Journal of Power Sources 163 (2006) 490–499.
[22] A.O. Omosun, A. Bauen, N.P. Brandon, C.S. Adjiman, D. Hart, Journal of Power Sources 131 (2004) 96–106.
[23] B. Tarroja, F. Mueller, J. Maclay, J. Brouwer, Journal of Engineering for Gas Turbines and Power 132 (2010) 072301.
[24] C.O. Colpan, I. Dincer, F. Hamdullahpur, International Journal of Hydrogen Energy 32 (2007) 787–795.
[25] C.O. Colpan, F. Hamdullahpur, I. Dincer, Y. Yoo, International Journal of Hydrogen Energy 35 (2010) 5001–5009.
[26] F. Mueller, R. Gaynor, A.E. Auld, J. Brouwer, F. Jabbari, G.S. Samuelsen, Journal of Power Sources 176 (2008) 229–239.
[27] F. Mueller, F. Jabbari, J. Brouwer, R. Roberts, T. Junker, H. Ghezel-Ayagh, Journal of Fuel Cell Science and Technology 4 (2007) 221–230.
[28] F. Mueller, B. Tarroja, J. Maclay, F. Jabbari, J. Brouwer, S. Samuelsen, Journal of Fuel Cell Science and Technology 7 (2010) 031007.
[29] R.A. Roberts, J. Brouwer, Journal of Fuel Cell Science and Technology 3 (2006) 18–25.
[30] F. Mueller, J. Brouwer, F. Jabbari, S. Samuelsen, Journal of Fuel Cell Science and Technology 3 (2006) 144–154.
[31] A. Martinez, K. Gerdes, R. Gemmen, J. Poston, Journal of Power Sources 195 (2010) 5206–5212.
[32] F. Calise, A. Palombo, L. Vanoli, Journal of Power Sources 158 (2006) 225–244.
[33] S.H. Chan, H.K. Ho, Y. Tian, Journal of Power Sources 109 (2002) 111–120.
[34] S.H. Chan, H.K. Ho, Y. Tian, Journal of Power Sources 114 (2003) 213–227.
[35] Y. Zhao, C. Ou, J. Chen, International Journal of Hydrogen Energy 33 (2008) 4161–4170.
[36] F. Calise, G. Restuccia, N. Sammes, Journal of Power Sources 195 (2010) 1163–1170.
[37] J. Sadhukhan, Y. Zhao, M. Leach, N.P. Brandon, N. Shah, Industrial and Engineering Chemistry Research 49 (2010) 11506–11516.
[38] F.A. Al-Sulaiman, I. Dincer, F. Hamdullahpur, International Journal of Hydrogen Energy 35 (2010) 5104–5113.
[39] F.A. Al-Sulaiman, I. Dincer, F. Hamdullahpur, Journal of Power Sources 195 (2010) 2346–2354.
[40] J. Sadhukhan, Y. Zhao, N. Shah, N.P. Brandon, Chemical Engineering Science 65 (2010) 1942–1954.
[41] S.H. Chan, C.F. Low, O.L. Ding, Journal of Power Sources 103 (2002) 188–200.
[42] R.T. Leah, N.P. Brandon, P. Aguiar, Journal of Power Sources 145 (2005) 336–352.
[43] S. Farhad, F. Hamdullahpur, Y. Yoo, International Journal of Hydrogen Energy 35 (2010) 3758–3768.
[44] E. Fontell, T. Kivisaari, N. Christiansen, J.B. Hansen, J. Pålsson, Journal of Power Sources 131 (2004) 49–56.
[45] R.C. Reid, J.M. Prausnitz, T.K. Sherwood, The Properties of Gases and Liquids, McGraw-Hill, New York, 1977.
[46] A. Lanzini, M. Santarelli, G. Orsello, Fuel Cells 10 (2010) 654–675.
[47] S. Gordon, B.J. McBride, Computer Program for Calculation of Complex Chemical Equilibrium Compositions and Applications. I. Analysis, NASA Lewis Research Center, 1994, http://www.grc.nasa.gov/www/CEAWEB.
[48] J.H. Horlock, Advanced Gas Turbine Cycles, Elsevier, Amsterdam/London, 2003.
[49] C. Wu, R.L. Kiang, Journal of Engineering for Gas Turbines and Power 113 (1991) 501–504.
[50] Y. Zhang, B. Lin, J. Chen, Renewable Energy 32 (2007) 856–867.
[51] Y. Haseli, I. Dincer, G.F. Naterer, Thermochimica Acta 480 (2008) 1–9.
[52] E. Baniasadi, A.A. Alemrajabi, International Journal of Hydrogen Energy 35 (2010) 9460–9467.
[53] A. Durmayaz, O.S. Sogut, B. Sahin, H. Yavuz, Progress in Energy and Combustion Science 30 (2004) 175–217.
[54] A. Arsalis, Journal of Power Sources 181 (2008) 313–326.
[55] D. Sánchez, A. Muñoz, T. Sánchez, Journal of Power Sources 169 (2007) 25–34.
[56] J.P. Trembly, R.S. Gemmen, D.J. Bayless, Journal of Power Sources 163 (2007) 986–996.
[57] A.V. Akkaya, B. Sahin, H. Huseyin Erdem, International Journal of Hydrogen Energy 33 (2008) 2566–2577.
[58] F. Calise, M. Dentice d'Accadia, A. Palombo, L. Vanoli, Energy 31 (2006) 3278–3299.
[59] X. Zhang, J. Li, G. Li, Z. Feng, Journal of Power Sources 164 (2007) 752–760.